Structural Properties of Rotating Hybrid Compact Stars with Color-Flavour-Locked Quarks Matter core and its Tidal Deformability

Suman Thakur* and Shashi K. Dhiman†

Department of Physics, Himachal Pradesh University,

Summer-Hill, Shimla - 171005, India.

(Dated: March 2, 2022)

Abstract

We investigate the possible sequels, for the hybrid compact stars consisting of nucleons, hyperons and three flavour color-flavor-locked quarks phase under global neutrality and chemical equilibrium conditions. The hadron equations of state are computed within the framework of energy density functionals based on the relativistic mean field theory by employing two different model parameterizations. The quarks matter phase of equation of state is computed by using Quarks Quasiparticle model derived from a non-relativistic energy density-functional approach. A plausible set of hybrid equations of state for superdense hadron-quarks matter is obtained and, which satisfies the constraints provided by bulk nuclear matter, the observational data of frequencies and maximum Gravitational mass $2M_{\odot}$ with their extracted radii, Keplerian limits, secular axisymmetric instability and limits of tidal deformabilities from GW170817 binary neutron stars (BNS) merger. We obtained structural properties of nonrotating and rotating compact stars, the evolutionary sequences with constant baryonic mass star spinning down by electromagnetic and gravitational radiations and, discuss the issues relating to phase transition from hadron to quarks matter phase. The internal structure of rotating star with observed spin down frequencies, exhibiting shrinkage of soft quarks core of compact stars are discussed for constant baryonic mass. We present the theoretically computed limits of radii for the spin down configurations of hybrid stars corresponding to the recently observed millisecond pulsars. We also present and discuss the calculated results for tidal deformability, Λ and tidal parameters Λ_1, Λ_2 of non spining hybrid star which are consistent with the waveform model analysis of GW170817 BNS.

* sumanthakur88@gmail.com

† shashi.dhiman@gmail.com

I. INTRODUCTION

It has been investigated [1–4] that the dense matter in the core of compact stars may consist of quark matter and, should be described as a color quarks as the fundamental degree of freedom. Therefore, the hybrid stars phenomenology offers a unique tool to address the challenge of understanding the phase transition in the dense quantum chromodynamics (QCD). Recently, the nuclear theory studies [5–7] are mainly in focus for understanding dense matter of compact stars (CS). Recent observations at LIGO and Virgo of GW170817 event [8, 9] identified as almost certainly the merger of Binary Neutron Stars and the discovery of CS with masses around $2M_{\odot}$ [10–12] have intensified the interest in these intriguing objects. The analysis GW170817 has demonstrated the potential of gravitational wave (GW) observations to yield new information relating to the limits on CS tidal deformability. In addition to these astrophysical observations [13–17] the measurements of rotation frequencies of the pulsar can be employ to constrain the composition and behaviour of Equations of State (EOS) of the dense nuclear matter. However, the direct measurement of radius of CS is still a great challenge from astrophysical observations. The upcoming high-precision x-ray space missions, such as the ongoing NICER (Neutron Star Interior Composition Explorer) [12, 16, 18] and the future eXTP (Enhanced X-ray Timing and Polarimetry Mission) [19] have aimed to improve the situation by simultaneous measurements of CS masses and radii with higher accuracy [20, 21]. It is also expected that limits on CS radii are to be improved by new detections of gravitational wave signals from neutron star mergers.

The investigations of the observed masses and extraction of the radii of CS would allow us to reveal composition and various phases of EOS of dense matter. Many attempts [17, 21, 22] have been made by using microscopic many body nuclear theories to model the nuclear matter EOS capable of constructing CS, containing nucleons, hyperons and quarks, under the constraint of global β-equilibrium. The EOS including hyperons and/or quarks are typically much softer than those containing just nucleons, leading to the reduction of maximum Gravitational masses of CS which may not be compatible with recent observations of $2M_{\odot}$. Whereas, the properties of the composition of EOS of CSs are not completely understood due to an apparent complications of non-perturbative effects of QCD. In the low energy regime the QCD coupling constant will be significantly large and experimental data have large uncertainties [23], therefore, it is not yet possible to obtained a reliable EOS of quark

matter phase from the first principle of QCD. The quarks matter phase of EOSs have been treated by employing phenomenological models with some basic features of QCD, such as, the MIT bag models [24–26] with a bag constant and appropriate perturbative QCD corrections and Nambu-Jona-Lasino with chiral symmetry and its breaking [27].

In the present work we compute a set of hybrid equations of state, where the hadron phase has been calculated within the framework of energy density functionals based on the relativistic mean field theory [22] and, the quarks matter phase of equation of state is computed by using Quarks Quasiparticle model QQPM [28] with CFL phase [25]. The medium effects are included in the cold quarks matter in terms of variation in effective mass of quarks and effective bag parameters as function of chemical potential. Further a plausible set of hybrid equations of state for hadron-quarks matter is employed to determine the maximum Gravitational mass, equatorial radius and rotation frequency of stable stellar configuration of hybrid stars, which satisfies the constraints provided by Keplerian limits, secular axisymmetric instability, the observational data of frequencies and maximum Gravitational mass $2M_{\odot}$ of static sequences with their radii and GW170817 event of neutron stars merger. We further constrain the radii of hybrid star to the recent limit extracted from GW170817 BNS R_1=$11.9^{+1.4}_{-1.4}$km and R_2 =$11.9^{+1.4}_{-1.4}$km. We presented the evolutionary sequences for hybrid CS with constant baryonic mass spinning down by electromagnetic and gravitational radiations and, discuss the issues relating to phase transition from hadron to quarks matter phase. The internal structure of rotating star with observed spin down frequencies, exhibiting shrinkage or expansion of soft core of star are discussed for constant baryonic mass. We present the theoretically computed limits for the results of spin down configurations of hybrid stars corresponding to the recently observed millisecond pulsars, for the Love number, k_2 and the tidal deformability, Λ. We approximate the hybrid star as a axisymmetric and rigid rotating body, and resort to Einstein's theory of general relativity for a rapidly rotating star. Recently, numerical methods for (axisymmetric) rotating stellar structure have been advanced by several groups [29–35]. In this work we employed the Rotating Neutron Star RNS method and code [29, 34] to calculated the properties of rapidly rotating Hybrid CSs.

The paper has been organised as, in section II, we described the theoretical framework employed to compute the hybrid EOSs. The Extended field-theoretical relativistic mean field (EFTRMF) models have been employed to describe the nucleons and hyperons phases and, whereas the quarks matter phase has been obtained from the QQPM. The mixed phase

of hybrid equations of state is obtained by using Glendenning construction based on Gibbs conditions of equilibrium. The framework of Relativistic Rotation of CSs are described in section III. The section IV, present results and discussions for equations of state employed to construct the non-rotating and rapidly rotating hybrid stars. The rotational evolution for a constant baryonic mass is also discussed. We have also presented and discussed the theoretical results of the tidal deformability of hybrid star in the context of GW17017 event of Neutron Stars merger. The conclusions of the present research works are presented in section V.

II. THEORETICAL FRAMEWORK

In this section, we discuss the theoretical approaches employed to the calculated sets of equations of state of dense nuclear matter in different phases. The EFTRMF model parameter BSR3 has been successfully applied in describing the nuclear structure properties of finite nuclei, properties of bulk nuclear matter at saturation densities, dense asymmetric nuclear matter, hadrons and hyperons nuclear matter at high densities [22]. These model parameters have been adopted to compute EOSs and construct neutron stars and hybrid CSs. The final hybrid EOS is comprised of two separate EOSs for each phase of matter, which are combined by utilising a Glendenning phase transition construction [36, 37].

A. Hadron Phase

In the EFTRMF model the effective Lagrangian density consists of self and mixed interaction terms for σ, ω, and ρ mesons upto the quartic order in addition to the exchange interaction of baryons with σ, ω, and ρ mesons. The σ, the ω, and the ρ mesons are responsible for the ground state properties of the finite and heavy nuclei. The mixed interactions terms containing the ρ-meson field enables us to vary the density dependence of the symmetry coefficient and neutron skin thickness in heavy nuclei over the wide range without affecting the other properties of the finite nuclei [38, 39]. In particular, the contribution from the self-interaction of ω-mesons peforms an important role in determining the high density behaviour of EOS and structure properties of compact stars [22, 40]. Whereas the inclusion of self-interaction of ρ-meson affect the ground state properties of heavy nuclei and compact

TABLE I. The coupling strength parameterizations of the Lagrangian density defined in Eq.(1) for BSR3[22] and IOPB I[41] models. The ω-meson self coupling ζ is equal to 0.0 for BSR3 and 0.0173436 for IOPB-I models, respectively. The masses of the mesons are taken to be m_ω = 782.5MeV, m_ρ = 763MeV, m^*_σ = 975MeV, and m_ϕ = 1020MeV for BSR3 parameterizations. The masses of the mesons are taken to be m_ω = 782.187MeV, m_ρ = 762.468MeV for IOPB-I parameterizations. The mass of nucleon, M_N =939MeV, and the masses of hyperons, M_Λ = 1116MeV, M_Σ = 1193MeV, and M_Ξ =1313MeV. The values of $\overline{\kappa}$, $\overline{\lambda}$, $\overline{\alpha_1}$, $\overline{\alpha_1}'$, $\overline{\alpha_2}$, $\overline{\alpha_2}'$ and $\overline{\alpha_3}'$ are multiplied by 10^2.

EOS	$\triangle$r	$g_{\sigma N}$	$g_{\omega N}$	$g_\rho N$	$\overline{\kappa}$	$\overline{\lambda}$	$\overline{\alpha_1}$	$\overline{\alpha_1}'$	$\overline{\alpha_2}$	$\overline{\alpha_2}'$	$\overline{\alpha_3}'$	m_σ
BSR3	0.20	10.4442	13.5223	13.1170	2.4304	-0.0427	0.1812	0.1597	2.9666	1.2530	0.0972	497.8348
IOPB-I	0.221	10.3966	13.3509	11.1257	1.8584	-0.7621	0.0	0.0	0.0	0.0	2.40	500.4870

stars only very marginally [40]. In the present work, We use only BSR3 parameterization to construct the hadronic phase of the Hybrid EOS. The Lagrangian density for the EFTRMF model can be written as

$$\mathcal{L} = \mathcal{L}_{\mathcal{BM}} + \mathcal{L}_\sigma + \mathcal{L}_\omega + \mathcal{L}_\rho + \mathcal{L}_{\sigma\omega\rho} + \mathcal{L}_{em} + \mathcal{L}_{e\mu} + L_{YY}, \tag{1}$$

A detailed description of each term of the effective Lagrangian density Eq.(1) is given in Ref. [22]. The equation of motion for baryons, mesons, and photons can be derived from the Lagrangian density defined in Eq.(1) by the Euler-Lagrange Principle [22].

The energy density of the uniform matter within the framework of EFTRMF model is

given by;

$$\begin{aligned}
\mathcal{E} &= \sum_{j=B,\ell} \frac{1}{\pi^2} \int_0^{k_j} k^2 \sqrt{k^2 + M_j^{*2}} dk \\
&+ \sum_B g_{\omega B} \omega \rho_B + \sum_B g_{\rho B} \tau_{3B} \rho + \frac{1}{2} m_\sigma^2 \sigma^2 \\
&+ \frac{\overline{\kappa}}{6} g_{\sigma N}^3 \sigma^3 + \frac{\overline{\lambda}}{24} g_{\sigma N}^4 \sigma^4 - \frac{\zeta}{24} g_{\omega N}^4 \omega^4 \\
&- \frac{\xi}{24} g_{\rho N}^4 \rho^4 - \frac{1}{2} m_\omega^2 \omega^2 - \frac{1}{2} m_\rho^2 \rho^2 \\
&- \overline{\alpha_1} g_{\sigma N} g_{\omega N}^2 \sigma \omega^2 - \frac{1}{2} \overline{\alpha_1}' g_{\sigma N}^2 g_{\omega N}^2 \sigma^2 \omega^2 \\
&- \overline{\alpha_2} g_{\sigma N} g_{\rho N}^2 \sigma \rho^2 - \frac{1}{2} \overline{\alpha_2}' g_{\sigma N}^2 g_{\rho N}^2 \sigma^2 \rho^2 \\
&- \frac{1}{2} \overline{\alpha_3}' g_{\omega N}^2 g_{\rho N}^2 \omega^2 \rho^2 + \sum_B g_{\phi B} \phi \rho_B \\
&+ \frac{1}{2} m_{\sigma^*}^2 \sigma^{*2} - \frac{1}{2} m_\phi^2 \phi^2.
\end{aligned} \tag{2}$$

The pressure of the uniform matter is given by

$$\begin{aligned}
P &= \sum_{j=B,\ell} \frac{1}{3\pi^2} \int_0^{k_j} \frac{k^4 dk}{\sqrt{k^2 + M_j^{*2}}} - \frac{1}{2} m_\sigma^2 \sigma^2 \\
&- \frac{\overline{\kappa}}{6} g_{\sigma N}^3 \sigma^3 - \frac{\overline{\lambda}}{24} g_{\sigma N}^4 \sigma^4 + \frac{\zeta}{24} g_{\omega N}^4 \omega^4 \\
&+ \frac{\xi}{24} g_{\rho N}^4 \rho^4 + \frac{1}{2} m_\omega^2 \omega^2 + \frac{1}{2} m_\rho^2 \rho^2 \\
&+ \overline{\alpha_1} g_{\sigma N} g_{\omega N}^2 \sigma \omega^2 + \frac{1}{2} \overline{\alpha_1}' g_{\sigma N}^2 g_{\omega N}^2 \sigma^2 \omega^2 \\
&+ \overline{\alpha_2} g_{\sigma N} g_{\rho N}^2 \sigma \rho^2 + \frac{1}{2} \overline{\alpha_2}' g_{\sigma N}^2 g_{\rho N}^2 \sigma^2 \rho^2 \\
&+ \frac{1}{2} \overline{\alpha_3}' g_{\omega N}^2 g_{\rho N}^2 \omega^2 \rho^2 - \frac{1}{2} m_{\sigma^*}^2 \sigma^{*2} \\
&+ \frac{1}{2} m_\phi^2 \phi^2.
\end{aligned} \tag{3}$$

The various properties associated with nuclear matter are obtained by using the parameter sets of Table I. The values of B/A, K, M_N^*, and ρ_{sat} for all these parameter sets lie in a narrow range. B/A=16.11$\pm$0.04MeV, K=230.24$\pm$9.80MeV, M_N^*/M_N=0.605$\pm$0.004, and ρ_{sat}=0.148$\pm$0.003fm^{-3}.

The composition of nuclear matter (for species i=n, p, Λ, Σ^-, Ξ^-, Ξ^0, e^-, μ^-) at fixed baryon number density ρ_B=$\sum_i B_i \rho_i$ are determined in such a way that the charge neutrality

condition,

$$\sum_i q_i \rho_i = 0, \tag{4}$$

and the chemical equilibrium conditions

$$\mu_i = B_i \mu_n - q_i \mu_e, \tag{5}$$

are satisfied.

where B_i and q_i denotes baryon number and electric charge of the species i.

B. Quarks Phase

In the last few years the study of color superconducting phase in quark-gluon plasma has been drawing a great interest in discussing the possible states of quark matter. At QCD perturbative regime the attractive quark interaction introduces instabilities in the Fermi surface, producing a gap in the quasiparticle energy spectrum. The total thermodynamical potential density of quarks matter may written as [25],

$$\Omega(\bar{\mu}, \mu_e) = \Omega_{QQPM}(\bar{\mu}) + \Omega(\mu_e) + \Omega_{CFL}(\bar{\mu}), \tag{6}$$

where the first term in Eq.(6) is obtained from the quarks, μ_e is the electron chemical potential, so second term is from electrons and third term is from CFL pairing contribution. The contribution to first term in Eq.(6) is given by [28],

$$\Omega_{QQPM} = -\frac{1}{\pi^2} \sum_i \frac{1}{8} \big[\nu_i \sqrt{\nu_i^2 + m_i^{*2}} (2\nu_i^2 - 3m_i^{*2}) + 3m_i^{*4} \ln\Big(\frac{\sqrt{\nu_i^2 + m_i^{*2}} + \nu_i}{m_i^*}\Big) \big], \tag{7}$$

The contribution to the second term in Eqn.(6) is given by,

$$\Omega(\mu_e) = \frac{1}{\pi^2} \int_0^{\sqrt{\mu_e^2 - m_e^2}} \nu^2 (\sqrt{\nu^2 + m_e^2} - \mu_e) d\nu \tag{8}$$

CFL Pairing term contribution is given by,

$$\Omega_{CFL}(\bar{\mu}) = -\frac{3\Delta^2 \bar{\mu}^2}{\pi^2}, \tag{9}$$

where Δ is CFL color superconducting gap parameter of CFL phase of quark matter. Medium effects play an important role in describing the properties of quarks matter via the concept of effective masses.

Effective mass is taken to be [42–44],

$$m_i^* = \frac{m_{i0}}{2} + \sqrt{\frac{m_{i0}^2}{4} + \frac{g^2\mu_i^2}{6\pi^2}}, \tag{10}$$

where m_{i0}, μ_i and g is the current quark mass, quark chemical potential, strong interaction coupling constant respectively. In actual practice the strong coupling constant is running [45–47] which is having a phenomenological expression such as

$$g^2(T,\mu_i) = \frac{48}{29}\pi^2\Big[\ln\Big(\frac{0.8\mu_i^2 + 15.622T^2}{\Lambda^2}\Big)\Big]^{-1}, \tag{11}$$

where Λ is the QCD scale-fixing parameter. In the present calculation, the value is taken to be 200MeV. In Fig.(1), variation in coupling strength parameter for the present case is shown. It is observed that range of coupling strength parameter is from 3 to 5 for the chemical potential lying in the range of (510-320)MeV approximately. Also, it is showing the decrease in interaction strength with increase in chemical potential [48]. At zero temperature, number densities for all three flavors of quarks considered are the same and can be obtained as

$$n_i = \frac{d_q\nu_f^3}{6\pi^2} + \frac{2\Delta^2\bar{\mu}}{\pi^2}, \tag{12}$$

with i = u, d, and s and $\nu_f = \nu_u = \nu_d = \nu_s$.

$$\nu_f = \Big[\Big(2\mu - \sqrt{\mu^2 + \frac{m_s^2 - m_u^2}{3}}\Big)^2 - m_u^2\Big], \tag{13}$$

for $\mu = \frac{\mu_u+\mu_d+\mu_s}{3}$ is common Fermi momentum of the quark system which depends on the mass of the three quark flavors.

For $m_u = m_d = 0$, common fermi momentum becomes,

$$\nu = 2\mu - \sqrt{\mu^2 + \frac{m_s^2}{3}}, \tag{14}$$

For the quarks matter the energy density becomes,

$$\begin{aligned}\mathcal{E}_{QM} = \frac{1}{\pi^2}\sum_i \frac{3}{8}\big[\nu_i\sqrt{\nu_i^2 + m_i^{*2}}(2\nu_i^2 + m_i^{*2}) \\ - m_i^{*4}\ln(\frac{\sqrt{\nu_i^2 + m_i^{*2}} + \nu_i}{m_i^*})\big] + B^*,\end{aligned} \tag{15}$$

Thus, pressure becomes

$$P_{QP} = -\Omega(\bar{\mu}, \mu_e) - B^*. \tag{16}$$

B^* is the effective Bag function and, can be written as,

$$B^* = \sum_i B_i(\mu_i) + B_0. \tag{17}$$

The introduction of B^* is done to shows the automatic confinement characteristic in the model, where B_0 is similar to the conventional MIT bag constant.
The μ_i-dependent part of effective bag function is calculated as,

$$B_i(\mu_i) = -\int_{m_i^*}^{\mu_i} \frac{\partial \Omega_i}{\partial m_i^*} \frac{\partial m_i^*}{\partial \mu_i} d\mu_i. \tag{18}$$

With the above quark mass formulae and thermodynamic treatment, one can get the properties of bulk CFL quark matter.
In the CFL phase, the three flavors of quarks satisfy the following conditions:
(i) they have equal fermi momenta, which minimizes the free energy of the system.
(ii) they have equal number densities n_i, as a consequence of the first condition, which means that $n_i = n_B$ and $\mu_i = \mu$, for i = u, d, s.

C. Mixed Phase

We construct the mixed phase of EOS made up of the hadron matter and quark matter by employing the Glendenning construction [36, 37] for hybrid compact star. The equilibrium chemical potential of the mixed phase corresponding to the intersection of the two surfaces representing hadron and quark phase can be calculated from the Gibbs condition for mechanical and chemical equilibrium at zero temperature which reads as,

$$P_{HP}(\mu_e, \mu_n) = P_{QP}(\mu, \mu_e) = P_{MP}, \tag{19}$$

In mixed phase, we considered chemical equilibrium at the hadron-quark interface as well as inside each phase [49], so that Eq.(5) implies

$$\mu_u + \mu_e = \mu_d = \mu_s, \tag{20}$$

$$\mu_p + \mu_e = \mu_n = \mu_\Lambda = \mu_{\Xi^0} = \mu_u + 2\mu_d, \tag{21}$$

$$\mu_{\Sigma^-} + \mu_p = 2\mu_n, \mu_{\Xi^-} + \mu_p = 2\mu_n. \tag{22}$$

In the mixed phase the local charge neutrality condition is replaced by the global charge neutrality which means that both hadron and quark matter are allowed to be charged separately. The condition of the global charge neutrality can be expressed as,

$$\chi\rho_c^{QP} + (1-\chi)\rho_c^{HP} = 0, \tag{23}$$

where, χ the volume fraction occupied by quark matter in the mixed phase in terms of charge density ρ_c. The value of the χ increases from zero in the pure hadron phase to $\chi = 1$ in the pure quark phase. The energy density $\mathcal{E}_{MP}$ and the baryon density ρ_{MP} of the mixed phase can be calculated as,

$$\mathcal{E}_{MP} = \chi\mathcal{E}_{\mathcal{QP}} + (1-\chi)\mathcal{E}_{HP}. \tag{24}$$

$$\rho_{MP} = \chi\rho_{QP} + (1-\chi)\rho_{HP}. \tag{25}$$

With the above evaluated hybrid star EOS presented, we can now analyse the structure of the rotating hybrid stars.

III. RELATIVISTIC ROTATION OF STARS

The structure of a rapidly rotating CS is different from the static one, since the roation can strongly deform the star. We assume CS are steadily rotating and have axisymmetric structure. Therefore the space-time metric used to model a rotating star can be expressed as,

$$\begin{aligned} ds^2 = &-e^{\gamma+\rho}dt^2 + e^{2\beta}(dr^2 + r^2 d\theta^2) \\ &+e^{\gamma-\rho}r^2\sin^2\theta(d\phi - \omega dt)^2, \end{aligned} \tag{26}$$

where the potentials γ, ρ, β, ω are functions of r and θ only. The matter inside the star is approximated by a perfect fluid and the energy-momentum tensor is given by,

$$T^{\mu\nu} = (\mathcal{E} + P)u^\mu u^\nu - Pg^{\mu\nu}, \tag{27}$$

where $\mathcal{E}$, P and u^μ are the energy density, pressure, and four-velocity, respectively. In order to solve Einstein's field equation for the potentials γ, ρ, β and ω, we adopt the KEH method [50] and use the RNS code [51] for calculating the properties of a rotating star. In Fig.(3), we present the results of the EOSs for the hybrid star and neutron star in the form P=P($\mathcal{E}$).

IV. RESULTS AND DISCUSSIONS

A. Equations of State and Non - rotating Hybrid Stars

In this section, we present the detail results for a set of EOSs of hybrid stars in the hadron phase, u, d, s quarks phase and mixed phase. In epitome, we employed Baym-Pethick-Sutherland EOS [52] for low density regime from outer crust baryon number density, $\rho_b = 6.3 \times 10^{-12}\text{fm}^{-3}$ upto the pasta phase $\rho_b = 9.4 \times 10^{-2}\text{fm}^{-3}$ that include the data and description of the neutron drip. In order to describe the EOS in liquid core of hybrid stars from its inner crust ρ_{crust} upto outer core $\rho_b \approx 0.35\text{fm}^{-3}$, we used an improved and consistent nuclear matter EOS in β-equilibrium based on Extended Field Theoretical Relativistic Mean Field model parameterizations BSR3 [22] and IOPB-I [41]. The coupling strength parameters of EFTRMF models for BSR3 and IOPB-I along with neutron skin thickness Δr of ^{208}Pb nucleus are presented in Table I of Section-II. These EFTRMF parmeterizations have successfully employed to investigate the experimental data of physical observables relating to the structural properties of finite nuclei [22, 41] and bulk properties of nuclear matter at saturation densities.

The set of EOSs employed in present work is presented in Table II, where the, Nucl1 and Nucl2 are the EOSs computed with parameters BSR3 and IOPB-I, respectively. The EOSs NHy1 and NHy2 are represented by the compositions of nucleons and hyperons, where hyperons appeared at a threshhold baryon number density $\rho_b \approx 0.35\text{fm}^{-3}$. In the present work, we have employed the values of hyperon-meson coupling parameters - $g_{mY_1} = 0.4714$, $g_{mY_2} = 0.9428$, $g_{\sigma^* Y_1} = -1.6666$, $g_{\sigma^* Y_2} = -1.3333$, $g_{\omega^* Y_1} = 0.8333$, $g_{\omega^* Y_2} = 0.4166$, $g_{\rho^*\Lambda} = g_{\rho^*\Sigma^0} = 0$ $g_{\rho^*\Sigma^-} = g_{\rho^*\Sigma^+} = 1$ $g_{\rho^*\Xi^-} = g_{\rho^*\Xi^0} = 0.5$ where Y_1 representing the hyperons as, Λ, Σ^-, Σ^+, Σ^0; Y_2 representing the hyperons Ξ^-, Ξ^0 and, m represent the σ and ω mesons. The EOSs presented in Table II as NmQ1, NmQ2 and NmQ3 are composed of nucleons and quarks in β-equilibrium with mixed phase of EOS varies from $\rho_b \approx 0.30$-0.40fm^{-3}, $\rho_b \approx 0.34$-0.50fm^{-3} and $\rho_b \approx 0.39$-0.52fm^{-3}. The description for the construction of mixed phase is discussed in Section (IIC). Finally, the EOS NHymQ4 has particle composition of nucleons, hyperons and quarks in β - equilibrium where the Λ hyperons are appeared at the threshold density of $\rho_b \approx 0.35\text{fm}^{-3}$ and the quarks phase transition occur at $\rho_b = 0.63\text{fm}^{-3}$. The quarks phase of hybrid EOS has been computed by employing Quark Quasiparticle model by

considering the color superconducting phase with CFL, Δ =50MeV. Whereas in the present calculation we consider all three quarks masses as, m_u=m_d=4MeV/c^2 and m_s=95MeV/c^2. In Table II, we list our EOSs and their particles composition, the brief description of theoretical models of dense matter and its parameters, the maximum gravitational mass, $M_G(M_\odot)$ of the compact stars, radius of the compact stars, R_{max}, baryon number density, ρ_b and energy density, $\mathcal{E}$ corresponding to maximum gravitational mass of the non-rotating compact stars. Therefore, in the present research work, for set of EOSs the Maximum gravitational mass of non-rotating hybrid stars varies in the range of (2.38-1.83)$M_\odot$ and radius varies as (11.76-12.08)km which satisfies the constraints of the recently extracted astrophysical observations of gravitational mass and radius of compact stars [53–56].

In Fig.(2), we present the variation of theoretically computed pressure (MeVfm^{-3}) as a function of energy density ε (MeVfm^{-3}) for the EOSs employed in the present work. In the upper panel, we present the EOSs Nucl1, Nucl2, NmQ1, NmQ2 and NmQ3 represented by black solid curve, brown dotted curve, orange double-dash-dotted curve, red small-dashed curve and indigo long dashed dotted curve respectively. The open coloured circles represent the boundaries of mixed phase consisting of nucleons and quarks in β-equilibrium. Further, the pressure at densities $2\rho_0$ and $6\rho_0$ of Nucl1 EOS are $5.25 \times 10^{34} dyne/cm^2$ and $9.648 \times 10^{35} dyne/cm^2$, respectively, are comparable with the recently measured pressure at same densities [8]. However, in the present work the magnitude of pressure is decreasing at $6\rho_0$, as the EOSs become softer with the appearance of hyperons and quarks matter phases and, the pressure at $6\rho_0$ for EOS of NHymQ4 model becomes $4.2 \times 10^{35} dyne/cm^2$.

In Fig.(3), we present the results for relationship between gravitational mass and radius of non-rotating compact star for various EOSs constructed in the present work. The region excluded by causality, light green solid line and rotation constraints of neutron star XTE J1739-285 solid maroon line are given. The mass and radius limit estimated from Vela pulsar glitches $\Delta I/I$=0.014 is shown as blue solid line. The mass limits of pulsars PSR J1614-2230 and PSR J0348+0432 are plotted for comparison. The limits on compact star mass and radius from Ozel's analysis of EXO 0748-676 with 1σ (dark solid black line) and 2σ, extended black line error bars are also shown. The mass radius relationship obtained from the EOS by extracted data of EOS by using QMC+Model A is also shown. The orange region bounded by the dotted maroon lines is representing the mass - radius relationship extracted for the proposed pulsar PSRJ0437-4715 for 3σ confidence level in the NICER

program [18]. The plausible set of EOSs used in the present calculation have bounds for maximum gravitational mass, $1.83M_{\odot}\leq$M$_G\leq$2.38M$_{\odot}$ and stars's radius, 11.76km-12.08km as shown in Table I, these limits of mass and radii are well within the recenlty extracted limits on mass and radii [53–55].

B. Rotating Hybrid Stars

The rotational frequency is a directly measurable physical quantity of the pulsars, and the Keplerian (mass-shedding) frequency f$_K$ is one of the most studied physical quantities for rotating stars [57–60]. In Table III, we present the structural properties of rotating compact stars at keplerain frequency. We present the values of maximum gravitational mass $M_{max}(M_{\odot})$, its corresponding equatorial radius R_{max}(km), central energy density $\mathcal{E}_c(\times 10^{15} g/cm^{-3})$, baryon density $\rho(fm^{-3})$, the maximum Keplerian frequency f_K(Hz) and the empirical approximation of maximum frequency f$_{max}$. The empirical formula [61] of f$_{max}$ is the correspondence between two extremal configurations of the static configuration with a maximum allowable mass, M$^{stat}_{max}$, R$^{stat}_{M_{max}}$, and stably rotating configuration with a maximum allowed frequency, can be written as,

$$f_{max} = f_0\Big(\frac{M^{stat}_{max}}{M_{\odot}}\Big)^{\frac{1}{2}}\Big(\frac{R^{stat}_{M_{max}}}{10km}\Big)^{(-\frac{3}{2})}, \tag{28}$$

where M$^{stat}_{max}$ and R$_{M_{max}}$ are the maximum gravitational mass and radius of the static configuration, respectively. The f$_0$ is a constant frequency equals to 1.22kHz, which does not depend on the theoretical model of EOS. This formula for f$_{max}$ is authentic for all CSs composition of hadrons in β- equilibrium, self-bound quarks matter stars and the hybrid compact stars. The Fig.(4), represent the theoretical results for the variation of gravitational mass as a function of equatorial radius for various model of EOSs. In Fig.(5), we presented keplerian frequency as a function of gravitational mass for EOSs used in the present work. It can be observed from Fig.(5) that the keplerian frequency increases monotonically both for hadronic star as well as hybrid star as a function of gravitational mass (M$_G$). The maximum gravitational mass and keplerian frequencies of the hybrid compact stars decreases as the hyperons and quarks appears in core of star and, consequently, the size of hybrid stars increases.

In order to visualize better the complex relations among M, R, and f$_K$, we present in Fig.(6) gravitational mass as a function of the equatorial radius at various fixed rotation

frequencies with EOS NHymQ4. The stable configurations are constrained by the kepler and SAI conditions at large and small radius, respectively. At a low frequency 465.1Hz, the lower boundary of mass M is fixed by the kepler condition and upper boundary by SAI condition. As the frequency of the known pulsars increases, f=465.1Hz [62], 641.9 Hz [63], 716.4Hz [64], 1122Hz [65], the SAI mark point moves more and more to the left side of the mathematical maximum. As the frequency increases further to f=1122Hz, the lower (upper) boundary values of mass M are fixed by the SAI (kepler) conditions. Also, the gravitational masses of the sequences as a function of equatorial radius for static, keplerian and evolutionary sequences is shown along with the evolutionary sequences.

C. Phase transition caused by rotational evolution

The possibility of a phase transition to quarks phase which is caused by the rotational evolution have been widely discussed in the literature [61, 66–69]. For a constant baryonic mass, a rotating star loses its rotational energy by magnetic dipole radiation, which makes the star spin-down and the central density increases. When the central density of a star reaches a critical value, the phase transition from the hadronic matter to quarks phase will take place, and star converts to a hybrid star. As the star continues spinning down and the central density continues increasing, more and more quarks matter phase appears in the core of the hybrid star. The Fig.(7) depicts the profile of the pressure as a function of equatorial distance of a compact star, whose rest mass is $2.226M_{\odot}$, on the internal radius of four spin frequencies in the range as, $0 \leq \nu \leq 716.4$Hz. For the frequency of fastest rotating stars 716Hz [64], it is found that the hybrid star do not contain quarks matter inside the core and it is composed of neutrons, protons and hyperons only. The stellar radius shrinks along with the regions of particles compositions of hyperons and mixed phase with the spin down frequencies and, however, the region of neutrons and protons expanded and quarks matter core appears at the frequency 465.1 Hz of pulsar [62]. At asymptotically slow rotation rates, the star represents a dense CFL quark phase that extends upto the radius 2.3km and, is surrounded by a mixed phase followed by hyperonic and nucleonic phase in the region between $2.3\text{km} \leq R \leq 12.07\text{km}$. Fig.(7) gives a true reflection of the internal structure of the stars as it spins-up or down, if the dynamical timescales are much larger than the timescales required for the nucleation of the CFL quarks matter phase.

D. The ms Pulsars and Limits of Radii

Recently, many attempts have been made to constrain the EOSs model with the extracted radii [17, 70–72] of compact stars from astrophysical observations by making use of various spectroscopic and timing methods. In this work we have attempted to predict the limits of radii of ms pulsars displayed in Table IV by employing the theoretical models NHymQ4 of EOS for hybrid star presented Table II. In Table IV, we present the catalogue of the recently observed pulsar's precise gravitational masses and their numerical computed spinning frequency in the range of 2.15ms-5.76ms. This knowledge of astrophysical data for mass and spin values of the pulsars may be enough to understand the behaviour of other compact stars, including some of the fast spinning accreting stars in LMXBs. In Table V, the theoretically computed limits for the results of spin-down sequences of hybrid star for gravitational mass $M_G(M_\odot)$, equatorial radii R_{eq}(km), baryonic mass M_B, redshift Z, moment of inertia I, the ratio of rotational to gravitational energies T/W, dimensionless angular momentum $cJ/GM_G{}^2$ and ratio of equatorial radii at pole to equator R_p/R_e are presented. The corresponding values of central energy density $e_c(\times 10^{15}\mathrm{gcm}^{-3})$ and baryon number density $\rho_c(\times 10^{14}\mathrm{gcm}^{-3})$ are also presented in the Table V. These limits for results have been obtained corresponding to the observed rotating frequencies ν at 465.1Hz, 416.7Hz, 366.0Hz, 339.0Hz, 317.5Hz, 315.5Hz, 287.4Hz, 279.3Hz and 173.6Hz corresponding to the pulsars shown in Table IV, PSR J1903+0327[13, 62], PSR J2043+1711[10, 16], PSR J0337+1715[73], PSR J1909-3744[74, 75], PSR J1614-2230[10, 16], PSR J1946+3417[17, 76], PSR J0751+1807[74, 77], PSR J2234+0611[17, 78] and PSR J0437-4715[79, 80].

The densest nuclear matter in the universe possibly nestles in the core of compact stars. Therefore, it is inveigling to know how dense matter can be for observed in ms pulsars with measured masses presented Table IV. These investigations will also characterise the compact star populations, and help us to understand their particles composition, formation and evolution. In view of recent astrophysical observations of pulsars with gravitational mass more than $1.4M_\odot$, the Fig.8, presents the theoretical limits of the radii of various well known millisecond pulsars presented in Table IV as a function of their rotating frequencies. The evolutionary sequences of the pulsars, theoretical limits of the radii and the gravitational mass of these pulsars have been computed by using NHymQ4 equation of state of hybrid star. For slow rotating hybrid star of gravitational maximum mass around $1.4M_\odot$, the limits

of the radii varies as 13.71km$\leq$R$_{eq}$ $\leq$14.10km which is very close with the recently extracted bounds on radii of the compact stars [6, 81]. Whereas for the spinning hybrid star with gravitational mass around 2.0M$_{\odot}$, we predict the limits of radii as, 12.85km$\leq$R$_{eq}$ $\leq$13.50km.

E. Static versus spinning configurations

In Table VI, we present the theoretically computed radii for the ms pulsars given in Table IV for non-spinning configurations, and the corresponding percentage bias in the allowed EOS of hybrid stars for model NHymQ4, if this model of EOS is constrained using an accurate $\pm$5% for equatorial radius measurement. For constraining EOS models using the radius measurements of radio ms pulsars, for example with NICER measurements, it is commonly argued that the comparably slow spin rates of compact stars nominally affect the radius. Nonetheless, the spin-related systematic error depends on the accuracy desired to measure the equatorial radius, R$_{eq}$ with desired accuracy of (ξ), as recommended about 5% [82]. NICER can also measure the stellar radius with a similar accuracy [18]. Therefore, we compute the radius R of ms pulsars for NHymQ4 EOS model for static configuration, and calculate the percentage difference η between R and R$_{eq}$ using the gravitational radii R for static configurations. If the EOS model is constrained using a R$_{eq}$ result measured with a percentage accuracy of $\pm$ ξ and using theoretical non-spinning configuration, then there can be ($\eta/2\xi$) $\times$ 100% of bias in the allowed EOS model. This means, $\sim$($\eta/2\xi$) $\times$ 100% of the allowed EOS models would be falsely allowed because of the systematic difference between R and R$_{eq}$. It can be noticed from the Table VI that the bias is quite high for the faster spinning pulsars for selected EOS model NHymQ4, whereas, the magnitude of the bias is smaller for slowly spinning pulsars. The computation of a bias will be indispensable to know the authenticity of constraints on EOS models. However, for a given η value, the ξ is expected to decrease with the availability of better instruments in the future. This will increase the bias values shown in Table VI, which shows the usefulness of the first extensive tabulation of these values and the computation of spinning configurations in the present work.

F. Tidal deformability

The dimensionless love number k_2 is an important physical quantity to measure the internal structure of the constituent body. The dimensionless tidal deformability parameter Λ depends on the neutron star compactness C and a dimensionless quantity k_2 as, $\Lambda=2k_2/3C^5$. To measure the love number k_2 along with the evaluation of the TOV equations we have to compute y=y(R) with initial boundary condition y(0)=2 from the first-order differential equation [83–86] iteratively,

$$y' = \frac{1}{r}[-r^2Q - ye^{\lambda}\{1 + 4\pi Gr^2(P - \mathcal{E})\} - y^2], \tag{29}$$

where $Q\equiv 4\pi G e^{\lambda}(5\mathcal{E}+9P+\frac{\mathcal{E}+P}{c_s^2})$ -$6\frac{e^{\lambda}}{r^2}$-ν'^2 and $e^{\lambda} \equiv (1 - \frac{2Gm}{r})^{-1}$ and, $\nu' \equiv 2\ G\ e^{\lambda}\ (\frac{m+4\pi Pr^3}{r^2})$. First, we get the solutions of Eq.(29) with boundary condition, $y=y_2(R)$, then the electric tidal Love numbers k_2 is calculated from the expression as,

$$\begin{aligned} k_2 = \frac{8}{5}(1-2C)^2[2C(y_2-1)-y_2+2]\{2C(4(y_2+1)C^4 \\ +(6y_2-4)C^3+(26-22y_2)C^2+3(5y_2-8)C-3y_2+6) \\ -3(1-2C)^2 \quad (2C(y_2-1)-y_2+2)\log(\frac{1}{1-2C})\}^{-1}. \end{aligned} \tag{30}$$

Fig.(9) right panel presents the dimensionless tidal love number k_2 as a function of gravitational mass of the compact star. The value of k_2 suddenly decreases with increasing gravitational mass from $0.95M_{\odot}$ onwards. The value of k_2 is low at higher and lower gravilational masses of the compact star and, indicating that the quadrupole deformation is maximum for intermediate ranges of masses. Fig.(9) left panel presents the dimensionless tidal deformability as a function of gravitational mass for the CS with selected eight EOSs in the present work. It is found that dimensionless tidal deformability decreases with increase in gravitational mass of compact stars. The obtained value of $\Lambda_{1.4}$ for 1.4 $M_{\odot}$ for selected EOSs is from $606M_{\odot}$ to $656M_{\odot}$, which is consistent with recent constraint proposed for tidal deformability $\Lambda_{1.4}$ from the GW170817 event [8, 87] for equation of state of dense nuclear matter. Finally, in Fig.(10) we plot the tidal deformability parameters Λ_1 and Λ_2 which have relationship with the neutron star binary companion having a high mass M_1 and a low mass M_2, repectively, associated with GW170817 event [9]. The dark green band and other colored solid line curves represents the tidal parameters for the representative set

of EOSs (see Table II) and other EOS model shown in Fig.(10), respectively. The curves of tidal parameters are ending at $\Lambda_1 = \Lambda_2$ boundary. The tidal parameters from RMF models IUFSU, TM1, and G2 are calculated by using our computer code and, the curves corresponding to the APR4 and SLy models are extracted from Fig.(1) [8] for comparison. The tidal parameters results are obtained by varying the high mass M_1 independently in the range as, 1.36 $\leq$M/M$_\odot$ $\leq$1.61 and, obtained the low mass partner M_2 of the neutron star merger by keeping the chirp mass $M_{chirp} = (M_1\ M_2)^{(3/5)}/(M_1 + M_2)^{1/5}$ fixed at the observed value, 1.186M$_\odot$ [9]. The low mass M_2 of the neutron binary is obtained in the range 1.16 $\leq$ M/M$_\odot$ $\leq$1.36, as presented in the Table VII for NHymQ4 EOS model. The long dashed black lines signifies the 50 % and the 90% probabilities of credible regions for waveform model TaylorF2 for low-spin priors [9]. Recently, LIGO and VIRGO detectors precisely measured the value of $\tilde{\Lambda}$ of the BNS [87]. The weighted dimensionless tidal deformability $\tilde{\Lambda}$ of the BNS of masses M_1 and M_1, and $\tilde{\Lambda} = \Lambda_1 = \Lambda_2$ is defined [87, 88] as,

$$\tilde{\Lambda} = \frac{16}{13}\left(\frac{(M_1 + 12M_2)M_1^4}{(M_1 + M_2)^5}\Lambda_1 + \frac{(M_2 + 12M_1)M_2^4}{(M_1 + M_2)^5}\Lambda_2\right), \tag{31}$$

with weighted tidal correction $\Delta\tilde{\Lambda}$ [89],

$$\Delta\tilde{\Lambda} = \frac{1}{2}\Big[\sqrt{1-4\eta}\Big(1 - \frac{13272}{1319}\eta + \frac{8944}{1319}\eta^2\Big)(\Lambda_1 + \Lambda_2) + \Big(1 - \frac{15910}{1319}\eta + \frac{32850}{1319}\eta^2 + \frac{3380}{1319}\eta^3\Big)(\Lambda_1 - \Lambda_2)\Big]. \tag{32}$$

Where $\eta = M_1M_2/M^2$ is the symmetric mass ratio and M = M_1 +M_2 is the total mass. The tidal parameters Λ_1 and Λ_2 satisfy the condition that the $M_1 \geq M_2$. In Table VII, we present the BNS masses M_1(M$_\odot$),M_2(M$_\odot$) and their corresponding radii R_1, R_2 in km, dimensionless tidal deformability parameters (Λ_1, Λ_2), weighted dimensionless tidal deformability $\tilde{\Lambda}$, tidal correction $\Delta\tilde{\Lambda}$ and chirp radius R_c in km for EOS model NHymQ4. Radius of chirp mass is $2M_{chirp}\tilde{\Lambda}^{1/5}$. It is noticed that the values of $\tilde{\Lambda} \leq 800$ in the low-spin priors, which is very well consistent with the recent observations [87]. The weighted tidal deformation is found to be lie in the range 689$\leq$ $\Delta\tilde{\Lambda}$ $\leq$732 and the chirp radius is in the range 8.77 km $\leq$$R_c$ $\leq$ 8.87 km for equal and unequal-mass binary neutron stars, as shown in Table VII.

V. CONCLUSIONS

In the present research work, we have obtained a plausible set of hybrid equations of state for superdense hadron-quarks matter which satisfies the constraints provided by finite nuclei, bulk nuclear matter, the observational data of frequencies and maximum gravitational mass $2M_{\odot}$ with their extracted radii, keplerian limits, secular axisymmetric instability and limits of tidal deformabilities from GW170817 BNS merger. The set of EOSs is constructed with the EFTRMF approach for hadronic matter and the QQPM model for quark matter, and assuming the phase transition under the Gibbs construction. Further, we considered in region of baryons densities as, $0 \leq \rho \leq 2\rho_0$, the EOS is composed of neutrons and protons in beta equilibrium, $2\rho \leq \rho \leq 4\rho_0$ hyperons appears and $4\rho_0 \leq \rho \leq 1.6fm^{-3}$ the quarks matter appears in β-equilibrium. The set of EOSs is used to determine the maximum gravitational mass, equatorial radius, rotation frequency of stable stellar configuration and tidal deformability of hybrid stars. Further, the hybrid EOS NHymQ4 model has been employed to investigate the phase transition cuased by the rotational evolution, the ms pulsars and limits of their radii and tidal deformability of hybrid CS.

We investigated the phase transition induced by the spin-down of pulsars with a constant baryonic mass $2.226\mathrm{M}_{\odot}$ on the internal radius of four spin frequencies in the range as, $0\leq \nu \leq$716.4Hz. It is found that the gravitational radius, regions of hadrons and mix phase of hybrid star shrinks with spin down frequencies and, the regions of nucleons matter and quarks matter expanded along the equatorial distance of the hybrid stars. However, for the frequency of fastest rotating stars 716Hz, the hybrid star do not contain quarks matter inside the core and it is composed of neutrons, protons and hyperons only and quarks matter core appears at the frequency 465.1 Hz of hybrid star. We computed and investigated the catalogue of the recently observed pulsars in terms of their structural properties and the results of spin-down sequences of hybrid star for gravitational mass $\mathrm{M}_G(M_{\odot})$, equatorial radii R_{eq}(km), baryonic mass M_B, redshift Z, moment of inertia I, ratio of rotational to gravitational energies T/W, dimensionless angular momentum $\mathrm{cJ/GM}_G{}^2$ and ratio of equatorial radii at pole to equator $\mathrm{R}_p/\mathrm{R}_e$. In case of recently observed pulsars with gravitational mass more than $1.4\mathrm{M}_{\odot}$, we have extracted the theoretical limits of the radii of various well known millisecond pulsars presented in Table IV as a function of their rotating frequencies by using NHymQ4 equation of state of hybrid star. For slowing rotating hybrid star of gravitational

maximum mass around $1.4M_{\odot}$, the limits of the radii varies as 13.71km$\leq R_{eq} \leq$14.10km which is very close with the recently extracted bounds on radii of the compact stars [6, 81]. Whereas for the spinning hybrid star with gravitational mass around $2.0M_{\odot}$, we predict the limits of radii as, 12.85km$\leq R_{eq} \leq$13.50km.

In the last we estimated love number and tidal deformability for the set of EOSs. The tidal deformability parameters do not differ much from each other for set of EOSs Fig.(10) and lie within the acceptable range as, $245 \leq \Lambda_1 \leq 732$ and $732 \leq \Lambda_2 \leq 1828$ and consistent with the associated components neutron binary stars of GW170817 event [9]. Further, by investigating the consequences of dimensionless tidal deformability $\Lambda_{1.4} \leq 800$ provided by LIGO-Virgo collaboration, we extract a limit of the stellar radius of neutron star of mass $1.4M_{\odot}$, $R_{1.4} \leq 13.24$km. The limits of radii suggested for binary neutron stars $R_1 = 11.9^{+1.4}_{-1.4}$ and $R_2 = 11.9^{+1.4}_{-1.4}$ from GW170817 event [9] implies that the EOS of dense nuclear matter at high densities is soft and, the evolution from stiff to soft EOS may indicate the phase transition in the interior of neutron star.

---

[1] E. Witten, Phys. Rev. D **30**, 272 (1984).

[2] E. Farhi and R. L. Jaffe, Phys. Rev. D **30**, 2379 (1984).

[3] P. Haensel, J. L. Zdunik, and R. Schaeffer, Astron. Astrophys. **160**, 121 (1986).

[4] C. Alcock, E. Farhi, and A. Olinto, Astrophys. J. **310**, 261 (1986).

[5] P. Haensel, A. Y. Potekhin, and D. G. Yakovlev, *Neutron stars 1: Equation of state and structure*, Vol. 326 (Springer Science & Business Media, 2007).

[6] J. M. Lattimer, Gen. Rel. Grav. **46**, 1713 (2014).

[7] G. Baym, T. Hatsuda, T. Kojo, P. D. Powell, Y. Song, and T. Takatsuka, Rep. Prog. Phys. **81**, 056902 (2018).

[8] B. P. Abbott, R. Abbott, T. D. Abbott, F. Acernese, K. Ackley, C. Adams, T. Adams, P. Addesso, R. Adhikari, V. Adya, *et al.*, Phys. Rev. Lett. **121**, 161101 (2018).

[9] B. P. Abbott, R. Abbott, T. D. Abbott, F. Acernese, K. Ackley, C. Adams, T. Adams, P. Addesso, R. Adhikari, V. Adya, *et al.*, Phys. Rev. X **9**, 011001 (2019).

[10] P. B. Demorest, T. Pennucci, S. M. Ransom, M. S. E. Roberts, and J. W. T. Hessels, nature **467**, 1081 (2010).

[11] J. Antoniadis, P. C. C. Freire, N. Wex, T. M. Tauris, R. S. Lynch, M. H. van Kerkwijk, M. Kramer, C. Bassa, V. S. Dhillon, T. Driebe, *et al.*, Science **340**, 1233232 (2013).

[12] Z. Arzoumanian, A. Brazier, S. Burke-Spolaor, S. Chamberlin, S. Chatterjee, B. Christy, J. M. Cordes, N. J. Cornish, F. Crawford, H. T. Cromartie, *et al.*, Astrophys. J. Suppl. S. **235**, 37 (2018).

[13] D. J. Champion, S. M. Ransom, P. Lazarus, F. Camilo, V. M. Kaspi, D. J. Nice, P. C. Freire, J. M. Cordes, J. W. Hessels, C. Bassa, *et al.*, in *AIP Conference Proceedings*, Vol. 983 (AIP, 2008) pp. 448–452.

[14] A. A. Abdo, M. Ackermann, M. Ajello, A. Allafort, E. Antolini, W. Atwood, M. Axelsson, L. Baldini, J. Ballet, G. Barbiellini, *et al.*, Astrophys. J. Suppl. S. **188**, 405 (2010).

[15] L. Guillemot, P. Freire, I. Cognard, T. Johnson, Y. Takahashi, J. Kataoka, G. Desvignes, F. Camilo, E. Ferrara, A. Harding, *et al.*, Mon. Not. R. astro. Soc. **422**, 1294 (2012).

[16] E. Fonseca, T. T. Pennucci, J. A. Ellis, I. H. Stairs, D. J. Nice, S. M. Ransom, P. B. Demorest, Z. Arzoumanian, K. Crowter, T. Dolch, *et al.*, Astrophys. J. **832**, 167 (2016).

[17] F. Özel and P. Freire, Annu. Rev. Astron. Astrophys. **54**, 401 (2016).

[18] K. C. Gendreau, Z. Arzoumanian, and T. Okajima, Proc. SPIE **8443**, 844313 (2012).

[19] S. N. Zhang and et al.(eXTP Collaboration), Proc. of SPIE-Int. Soc. Opt. Eng. **9905**, 914420 (2014).

[20] A. L. Watts, N. Andersson, D. Chakrabarty, M. Feroci, K. Hebeler, G. Israel, F. K. Lamb, M. C. Miller, S. Morsink, F. Özel, A. Patruno, J. Poutanen, D. Psaltis, A. Schwenk, A. W. Steiner, L. Stella, L. Tolos, and M. van der Klis, Rev. Mod. Phys. **88**, 021001 (2016).

[21] M. Oertel, M. Hempel, T. Klähn, and S. Typel, Rev. Mod. Phys. **89**, 015007 (2017).

[22] S. K. Dhiman, R. Kumar, and B. K. Agrawal, Phys. Rev. C **76**, 045801 (2007).

[23] S. Bethke, Prog. Part. Nucl. Phys. **58**, 351 (2007).

[24] M. Alford, M. Braby, M. Paris, and S. Reddy, Astrophys. J. **629**, 969 (2005).

[25] B. K. Agrawal and S. K. Dhiman, Phys. Rev. D **79**, 103006 (2009).

[26] E.-P. Zhou, X. Zhou, and A. Li, Phys. Rev. D **97**, 083015 (2018).

[27] D. P. Menezes, C. Providência, and D. Melrose, J. Phys. G Nucl. Part. Phys. **32**, 1081 (2006).

[28] C. J. Xia, G. X. Peng, S. W. Chen, Z. Y. Lu, and J. F. Xu, Phys. Rev. D **89**, 105027 (2014).

[29] H. Komatsu, Y. Eriguchi, and I. Hachisu, Mon. Not. R. astro. Soc. **239**, 153 (1989).

[30] F. Weber and N. Glendenning, Phys. lett. B **265**, 1 (1991).

[31] G. B. Cook, S. L. Shapiro, and S. A. Teukolsky, Astrophys. J. **398**, 203 (1992).

[32] G. B. Cook, S. L. Shapiro, and S. A. Teukolsky, Astrophys. J. **424**, 823 (1994).

[33] M. Salgado, S. Bonazzola, E. Gourgoulhon, and P. Haensel, Astron. Astrophys. **291**, 155 (1994).

[34] N. Stergioulas and J. L. Friedman, Astrophys. J. **444**, 306 (1995).

[35] N. Stergioulas, Living Reviews in Relativity **6**, 3 (2003).

[36] N. K. Glendenning, Phys. Rev. D **46**, 1274 (1992).

[37] N. K. Glendenning, Springer-Verlag, New York (2000).

[38] R. J. Furnstahl, Nucl. Phys. A **706**, 85 (2002).

[39] T. Sil, M. Centelles, X. Vinas, and J. Piekarewicz, Phys. Rev. C **71**, 045502 (2005).

[40] H. Mueller and B. D. Serot, Nucl. Phys. A **606**, 508 (1996).

[41] B. Kumar, S. K. Patra, and B. K. Agrawal, Phys. Rev. C **97**, 045806 (2018).

[42] K. Schertler, C. Greiner, and M. H. Thoma, Nucl. Phys. A **616**, 659 (1997).

[43] K. Schertler, C. Greiner, and M. H. Thoma, J. Phys. G: Nucl. Part. Phys **23**, 2051 (1997).

[44] R. D. Pisarski, Nucl. Phys. A **498**, 423 (1989).

[45] D. V. Shirkov and I. L. Solovtsov, Phys. Rev. Lett. **79**, 1209 (1997).

[46] X. J. Wen, J. Y. Li, J. Q. Liang, and G. X. Peng, Phys. Rev. C **82**, 025809 (2010).

[47] B. K. Patra and C. P. Singh, Phys. Rev. D **54**, 3551 (1996).

[48] H. Stocker, Nucl. Phys. A **418**, 587c (1984).

[49] T. Maruyama, S. Chiba, H.-J. Schulze, and T. Tatsumi, Phys. Rev. D **76**, 123015 (2007).

[50] H. Komatsu, Y. Eriguchi, and I. Hachisu, Mon. Not. R. Astron. Soc. **239**, 153 (1989).

[51] http://www.gravity.phys.uwm.edu/rns/.

[52] G. Baym, C. Pethick, and P. Sutherland, Astrophys. J. **170**, 299 (1971).

[53] E. R. Most, L. R. Weih, L. Rezzolla, and J. Schaffner-Bielich, Phys. Rev. Lett. **120**, 261103 (2018).

[54] E. Annala, T. Gorda, A. Kurkela, and A. Vuorinen, Phys. Rev. Lett. **120**, 172703 (2018).

[55] S. Bose, K. Chakravarti, L. Rezzolla, B. S. Sathyaprakash, and K. Takami, Phys. Rev. Lett. **120**, 031102 (2018).

[56] L. Rezzolla, E. R. Most, and L. R. Weih, Astrophys. J. Lett. **852**, L25 (2018).

[57] A. Zacchi, M. Hanauske, and J. Schaffner-Bielich, Phys. Rev. D **93**, 065011 (2016).

[58] M. G. Alford, G. F. Burgio, S. Han, G. Taranto, and D. Zappalà,

Phys. Rev. D **92**, 083002 (2015).

[59] J. M. Lattimer and M. Prakash, Phys. Rep. **442**, 109 (2007).

[60] O. Benhar, V. Ferrari, L. Gualtieri, and S. Marassi, Phys. Rev. D **72**, 044028 (2005).

[61] P. Haensel, M. Bejger, M. Fortin, and L. Zdunik, Eur. Phys. J. A **52**, 59 (2016).

[62] P. C. C. Freire, C. G. Bassa, N. Wex, I. H. Stairs, D. J. Champion, S. M. Ransom, P. Lazarus, V. M. Kaspi, J. W. T. Hessels, M. Kramer, *et al.*, Mon. Not. R. Astro. Soc. **412**, 2763 (2011).

[63] J. L. Friedman, J. N. Imamura, R. H. Durisen, and L. Parker, Nature **336**, 560 (1988).

[64] J. W. T. Hessels, S. M. Ransom, I. H. Stairs, P. C. C. Freire, V. M. Kaspi, and F. Camilo, Science **311**, 1901 (2006).

[65] P. Kaaret, Z. Prieskorn, S. Brandt, N. Lund, S. Mereghetti, D. Götz, E. Kuulkers, J. Tomsick, *et al.*, Astrophys. J. Lett. **657**, L97 (2007).

[66] M. Marczenko, D. Blaschke, K. Redlich, and C. Sasaki, Phys. Rev. D **98**, 103021 (2018).

[67] J. B. Wei, H. Chen, G. F. Burgio, H. J. Schulze, *et al.*, Phys. Rev. D **96**, 043008 (2017).

[68] N. S. Ayvazyan, G. Colucci, D. H. Rischke, and A. Sedrakian, A & A **559**, A118 (2013).

[69] J. L. Zdunik, M. Bejger, P. Haensel, and E. Gourgoulhon, A. & A. **450**, 747 (2006).

[70] B. Gendre, D. Barret, and N. Webb, A. & A. **403**, L11 (2003).

[71] S. Bhattacharyya, T. E. Strohmayer, M. C. Miller, and C. B. Markwardt, Astrophys. J. **619**, 483 (2005).

[72] S. Bogdanov, G. B. Rybicki, and J. E. Grindlay, Astrophys. J. **670**, 668 (2007).

[73] S. M. Ransom, I. Stairs, A. Archibald, J. Hessels, D. Kaplan, M. van Kerkwijk, J. Boyles, A. Deller, S. Chatterjee, A. Schechtman-Rook, *et al.*, Nature **505**, 520 (2014).

[74] B. A. Jacoby, M. Bailes, M. Van Kerkwijk, S. Ord, A. Hotan, S. Kulkarni, and S. Anderson, Astrophys. J. Lett. **599**, L99 (2003).

[75] G. Desvignes, R. N. Caballero, L. Lentati, J. P. W. Verbiest, D. J. Champion, B. W. Stappers, G. H. Janssen, P. Lazarus, S. Osłowski, S. Babak, *et al.*, Mon. Not. R. Astro. Soc. **458**, 3341 (2016).

[76] E. D. Barr, D. J. Champion, M. Kramer, R. P. Eatough, P. C. Freire, R. Karuppusamy, K. Lee, J. P. Verbiest, C. G. Bassa, A. G. Lyne, *et al.*, Mon. Not. R. Astro. Soc. **435**, 2234 (2013).

[77] S. C. Lundgren, A. F. Zepka, and J. M. Cordes, IAUC **5878** (1993).

[78] J. S. Deneva, K. Stovall, M. A. McLaughlin, S. D. Bates, P. C. C. Freire, J. G. Martinez,

F. Jenet, and M. Bagchi, Astrophys. J. **775**, 51 (2013).

[79] S. Johnston, D. Lorimer, P. Harrison, M. Bailes, A. Lynet, J. Bell, V. Kaspi, R. Manchester, N. D'Amico, L. Nleastrol, *et al.*, Nature **361**, 613 (1993).

[80] D. Reardon, G. Hobbs, W. Coles, Y. Levin, M. Keith, M. Bailes, N. Bhat, S. Burke-Spolaor, S. Dai, M. Kerr, *et al.*, Mon. Not. R. Astron. Soc. **455**, 1751 (2015).

[81] S. Bhattacharyya, I. Bombaci, D. Bandyopadhyay, A. V. Thampan, and D. Logoteta, New Astron. **54**, 61 (2017).

[82] J. M. Lattimer and M. Prakash, Astrophys. J. **550**, 426 (2001).

[83] T. Hinderer, Astrophys. J. **677**, 1216 (2008).

[84] T. Hinderer, Astrophys. J. **697**, 964 (2009).

[85] T. Hinderer, B. D. Lackey, R. N. Lang, and J. S. Read, Phys. Rev. D **81**, 123016 (2010).

[86] T. Damour and A. Nagar, Phys. Rev. D. **81**, 084016 (2010).

[87] B. P. Abbott, R. Abbott, T. Abbott, F. Acernese, K. Ackley, C. Adams, T. Adams, P. Addesso, R. Adhikari, V. Adya, *et al.*, Phys. Rev. Lett. **119**, 161101 (2017).

[88] M. Favata, Phys. Rev. lett. **112**, 101101 (2014).

[89] L. Wade, J. D. Creighton, E. Ochsner, B. D. Lackey, B. F. Farr, T. B. Littenberg, and V. Raymond, Phys. Rev. D **89**, 103012 (2014).

[90] J. Nattila, A. W. Steiner, J. J. E. Kajava, V. F. Suleimanov, and J. Poutanen, Astron. Astrophys. **591**, A25 (2016).

TABLE II. The equations of state and its particles composition, the brief description theoretical models of dense matter and its parameters, the maximum gravitational mass, $M_G(M_\odot)$ of the compact stars, maximum radius of the compact stars, R_{max} and energy density, $\mathcal{E}$ corresponding to maximum gravitational mass of the nonrotating compact stars. The data of EOSs are available with authors through email.

No.	EOS	Composition and Brief description Model	Maximum non - spinning mass ($M_\odot$)	R_{max}(km)	$\mathcal{E}(\times 10^{15} g/cm^{-3})$
1	Nucl1	n,p; BSR3	2.38	12.02	1.955
2	Nucl2	n,p;IOPB-I	2.16	12.07	1.92
3	NHy1	n, p, Λ,Σ,Ξ; BSR3	1.99	11.58	2.196
4	NHy2	n, p, Λ,Σ,Ξ, IOPB-I	1.83	11.76	2.08
5	NmQ1	n, p, u, d, s Δ = 50MeV,BSR3 $(B_0)^{1/4}$=150MeV	1.93	11.90	2.028
6	NmQ2	n, p, u, d, s Δ = 50MeV,BSR3 $(B_0)^{1/4}$=155MeV	1.89	12.0	1.978
7	NmQ3	n, p, u, d, s Δ = 50MeV,IOPB-I $(B_0)^{1/4}$=155MeV	1.85	11.75	2.07
8	NHymQ4	n, p, Λ,Σ,Ξ +u,d,s quarks Δ = 50MeV $(B_0)^{1/4}$=150MeV, BSR3	1.95	12.08	1.945

TABLE III. The structural properties of rotating compact stars, the maximum gravitational mass $M_{max}(M_\odot)$ and its corresponding equatorial radius R_{max}(km), central energy density $\mathcal{E}_c(\times 10^{15} g/cm^{-3})$, the maximum Keplerian frequency f_K(Hz), the approximate value of maximum frequency f_{max} as defined in Eq.(28).

		Nucl1	Nucl2	NHy1	NHy2	NmQ1	NmQ2	NmQ3	NHymQ4
Keplerian	$M_{max}/M_\odot$	2.87	2.60	2.39	2.20	2.32	2.28	2.52	2.37
	R_{max}(km)	16.06	16.26	16.22	16.57	16.42	16.95	16.73	16.75
	$\mathcal{E}_c(\times 10^{15} g/cm^{-3})$	1.67	1.70	1.75	1.67	1.72	1.57	1.53	1.61
	f_K(Hz)	1488	1396	1352	1261	1313	1245	1309	1288
	$\mathrm{f}_{max}(Hz)$	1428	1352	1381	1294	1306	1273	1303	1283

TABLE IV. List of ms pulsars with measured gravitational mass and less than 10 ms spin-period

No.	Pulsar name	Spin-period [frequency] (ms [Hz])	Mass ($\mathrm{M}_\odot$)	References
1	J1903+0327	2.15 [465.1]	$1.667^{+0.021}_{-0.021}$	[13, 62]
2	J2043+1711	2.40 [416.7]	$1.410^{+0.21}_{-0.18}$	[14–16]
3	J0337+1715	2.73 [366.0]	$1.4378^{+0.0013}_{-0.0013}$	[73]
4	J1909-3744	2.95[339.0]	$1.540^{+0.027}_{-0.027}$	[74, 75]
5	J1614-2230	3.15 [317.5]	$1.928^{+0.017}_{-0.017}$	[10, 16]
6	J1946+3417	3.17 [315.5]	$1.832^{+0.028}_{-0.028}$	[17, 76]
7	J0751+1807	3.48 [287.4]	$1.640^{+0.15}_{-0.15}$	[74, 77]
8	J2234+0611	3.58 [279.3]	$1.393^{+0.013}_{-0.013}$	[17, 78]
9	J0437-4715	5.76 [173.6]	$1.440^{+0.07}_{-0.07}$	[79, 80]

TABLE V. The theoretically computed limits for the results of spin down sequences of hybrid star for gravitational mass $M_G(M_\odot)$, equatorial radii R_{eq}(km), baryon mass M_B, redshift Z, moment of inertia, the ratio of rotational to gravitational energies T/W, dimensionless angular momentum $cJ/GM_G{}^2$ and ratio of equatorial radii at pole to equator. These limits for results have been obtained corresponding to the observed rotating frequencies ν at 465.1Hz, 416.7Hz, 366.0Hz, 339.0Hz, 317.5Hz, 315.5Hz, 287.4Hz, 279.3Hz and 173.6Hz corresponding to pulsars PSR J1903+0327[13, 62], PSR J2043+1711[10, 16],PSR J0337+1715[73], PSR J1909-3744[74, 75], PSR J1614-2230[10, 16],PSR J1946+3417[17, 76], PSR J0751+1807[74, 77], PSR J2234+0611[17, 78] andPSR J0437-4715[79, 80]. The corresponding values of central energy density $e_c = (\times 10^{15} gcm^{-3})$ and baryon number density $\rho_c(\times 10^{14}\mathrm{gcm}^{-3})$ are also shown in the table.

PSR J1903+0327, ν=465.1Hz, $M_G=1.667^{+0.021}_{-0.021}$								
ρ_c	e_c	$M_B(M_\odot)$	R_{eq}(km)	Z	$I(\times 10^{45}\mathrm{gcm}^2)$	T/W	$cJ/GM_G{}^2$	R_p/R_e
6.50	$0.75^{+0.02}_{-0.02}$	$1.84^{+0.03}_{-0.03}$	$14.07^{-0.03}_{+0.03}$	$0.26^{+0.00}_{-0.00}$	$2.39^{+0.03}_{-0.03}$	0.02	$0.79^{+0.01}_{-0.01}$	0.91
PSR J2043+1711, ν=416.7Hz, $M_G=1.41^{+0.21}_{-0.18}$								
5.36	$0.60^{+0.12}_{-0.06}$	$1.53^{+0.26}_{-0.21}$	$14.12^{-0.12}_{+0.08}$	$0.20^{+0.04}_{-0.03}$	$1.90^{+0.38}_{-0.32}$	0.02	$0.57^{+0.11}_{-0.09}$	0.91
PSR J0337+1715, ν=366.0Hz, $M_G=1.4378^{+0.0013}_{-0.0013}$								
5.53	$0.61^{+0.00}_{-0.00}$	$1.57^{+0.00}_{-0.00}$	$13.99^{-0.00}_{+0.00}$	$0.21^{+0.00}_{-0.00}$	$1.93^{+0.00}_{-0.00}$	0.01	$0.51^{+0.00}_{-0.00}$	0.93
PSR J1909-3744, ν=339.0Hz, $M_G=1.540^{+0.027}_{-0.027}$								
6.0	$0.67^{+0.02}_{-0.02}$	$1.69^{+0.03}_{-0.04}$	$13.90^{-0.01}_{+0.01}$	$0.23^{+0.01}_{-0.01}$	$2.11^{+0.05}_{-0.05}$	0.01	$0.51^{+0.01}_{-0.01}$	0.94
PSR J1614-2230, ν=317.5Hz, $M_G=1.928^{+0.017}_{-0.017}$								
10.56	$1.30^{+0.09}_{-0.07}$	$2.18^{+0.02}_{-0.02}$	$12.98^{-0.13}_{+0.11}$	$0.34^{+0.01}_{-0.01}$	$2.53^{-0.02}_{+0.01}$	0.01	$0.57^{-0.00}_{+0.00}$	0.96
PSR J1946+3417, ν=315.5Hz, $M_G=1.832^{+0.028}_{-0.028}$								
8.61	$1.03^{+0.06}_{-0.05}$	$2.06^{+0.04}_{-0.04}$	$13.43^{-0.10}_{+0.09}$	$0.30^{+0.01}_{-0.01}$	$2.51^{+0.02}_{-0.02}$	0.01	$0.57^{+0.00}_{-0.01}$	0.96
PSR J0751+1807, ν=287.4Hz, $M_G=1.64^{+0.15}_{-0.15}$								
6.66	$0.76^{+0.20}_{-0.12}$	$1.81^{+0.19}_{-0.18}$	$13.76^{-0.25}_{+0.08}$	$0.25^{+0.04}_{-0.03}$	$2.26^{+0.20}_{-0.26}$	0.01	$0.47^{+0.04}_{-0.05}$	0.96
PSR J2234+0611, ν=279.3Hz, $M_G=1.393^{+0.013}_{-0.013}$								
5.36	$0.60^{+0.00}_{-0.00}$	$1.51^{+0.02}_{-0.02}$	$13.85^{-0.00}_{+0.00}$	$0.20^{+0.00}_{-0.00}$	$1.82^{+0.02}_{-0.02}$	0.01	$0.36^{+0.00}_{-0.00}$	0.95
PSR J0437-4715, ν=173.6Hz, $M_G=1.44^{+0.07}_{-0.07}$								
5.53	$0.62^{+0.04}_{-0.02}$	$1.57^{+0.08}_{-0.08}$	$13.72^{-0.01}_{+0.01}$	$0.21^{+0.01}_{-0.01}$	$1.89^{+0.13}_{-0.12}$	0.00	$0.23^{+0.02}_{-0.02}$	0.97

TABLE VI. The theoretically computed radii of catalogued in Table IV for non-spinning configurations, and the corresponding percentage bias in the allowed EOS of hybrid stars for model NHymQ4, if this model of EOS is constrained using an accurate ±5% for equatorial radius measurement.

No.	$M_G(M_\odot)$	ν(Hz)	R(km)	R_{eq}	Bias(%)
1	1.667	465.1	13.47	14.07	42.6
2	1.41	416.7	13.57	14.12	38.4
3	1.4378	366.0	13.57	13.99	29.5
4	1.540	339.0	13.56	13.90	24.2
5	1.928	317.5	12.59	12.98	29.4
6	1.832	315.5	13.11	13.43	23.4
7	1.64	287.4	13.50	13.76	18.6
8	1.393	279.3	13.57	13.85	19.7
9	1.44	173.6	13.57	13.72	10.4

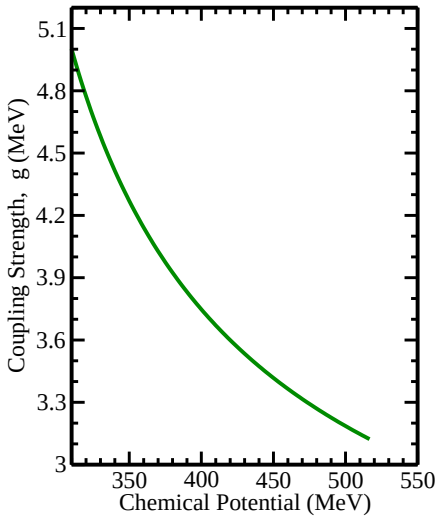

FIG.1

FIG. 1. Variation in Coupling strength parameter with chemical potential for Quarks Phase.

TABLE VII. The binary neutron star masses ($M_1(M_0)$, $M_2(M_0)$) and corresponding radii (R_1(km), R_2(km)), dimensionless tidal deformabilities (Λ_1,Λ_2), weighted dimensionless tidal deformability $\tilde{\Lambda}$,tidal correction $\Delta\tilde{\Lambda}$ and chirp radius R_c(km) for EOS NHymQ4.

M_1	M_2	R_1	R_2	Λ_1	Λ_2	$\tilde{\Lambda}$	$\Delta\tilde{\Lambda}$	R_c
1.36	1.36	13.61	13.24	745.81	732.13	731	-4.65	8.87
1.38	1.35	13.24	13.24	689.22	791.99	729	13.38	8.86
1.40	1.33	13.13	13.24	624.36	865.55	732	33.79	8.87
1.42	1.31	13.24	13.24	576.46	937.39	728	49.59	8.86
1.44	1.29	13.24	13.24	526.85	1010.95	726	66.11	8.86
1.46	1.27	13.13	13.24	485.80	1093.60	729	81.93	8.86
1.48	1.26	13.24	13.34	446.46	1182.86	728	98.46	8.86
1.50	1.24	13.34	13.24	408.83	1270.10	722	113.66	8.85
1.52	1.22	13.24	13.34	374.62	1354.77	715	127.10	8.83
1.54	1.21	13.24	13.34	345.54	1462.71	724	142.61	8.85
1.56	1.19	13.13	13.34	316.46	1570.30	717	157.44	8.83
1.58	1.18	13.13	13.34	289.09	1677.04	718	171.04	8.83
1.60	1.17	13.13	13.34	263.43	1777.80	704	182.64	8.80
1.61	1.16	13.43	13.57	245.63	1828.60	689	189.95	8.77

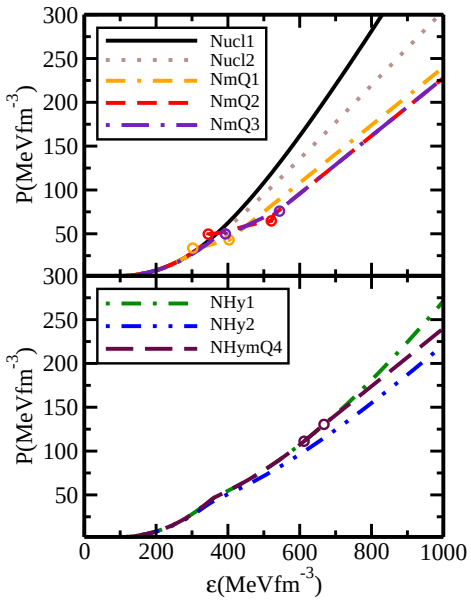

FIG.2

FIG. 2. The variation of pressure (MeVfm^{-3}) as a function of energy density ε (MeVfm^{-3}) for various selected EOSs.

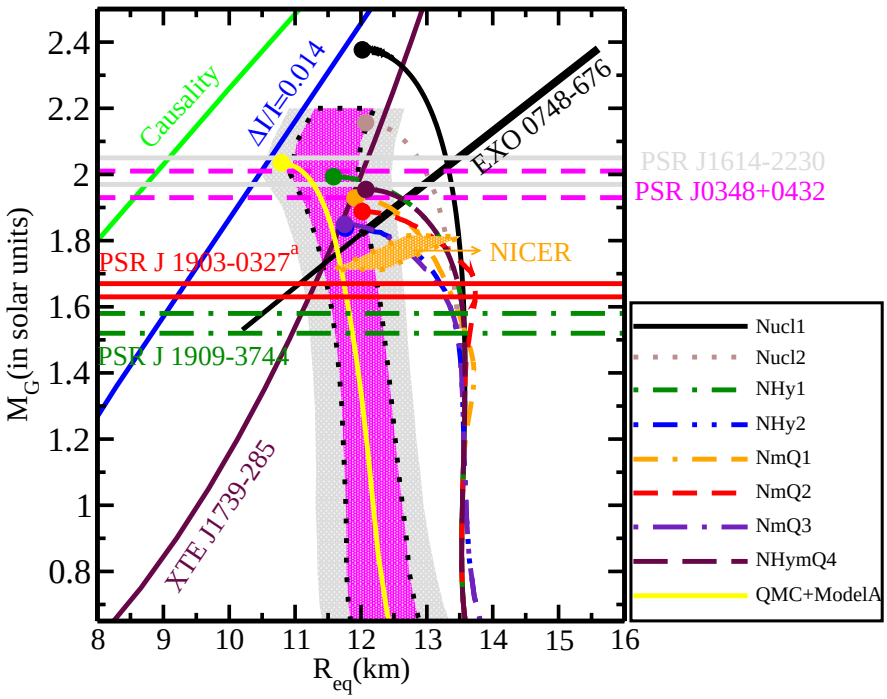

FIG.3

FIG. 3. Relationship between gravitational mass and radius of non - rotating compact star for various EOSs. The region excluded by causality light green solid line and rotation constraints of neutron star XTE J1739-285 solid maroon line are given. The mass and radius limit estimated from Vela pulsar glitches $\Delta I/I$=0.014 is shown as blue solid line. The mass limits of pulsars PSR J1614-2230 and PSR J0348+0432 are plotted for comparison. The limits on compact star mass and radius from Ozel's analysis of EXO 0748-676 with 1σ (dark solid black line) and 2σ (extended black line) error bars are also shown. The mass radius relationship obtained in Ref.[90] from extracted data of EOS by using QMC+Model A. The orange region bounded by the dotted maroon lines is representing the mass - radius relationship extracted for the proposed pulsar PSRJ0437-4715 for 3σ confidence level in the NICER program [18].

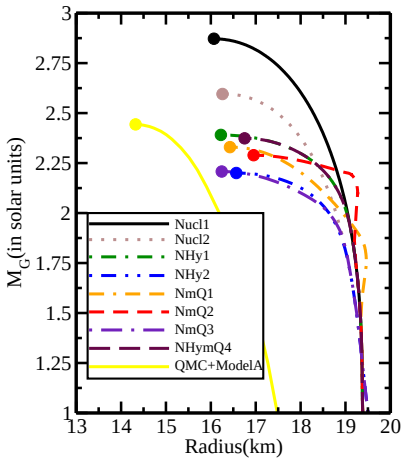

FIG.4

FIG. 4. The variation of gravitational mass as a function of equatorial radius with Keplerian configurations for various EOSs.

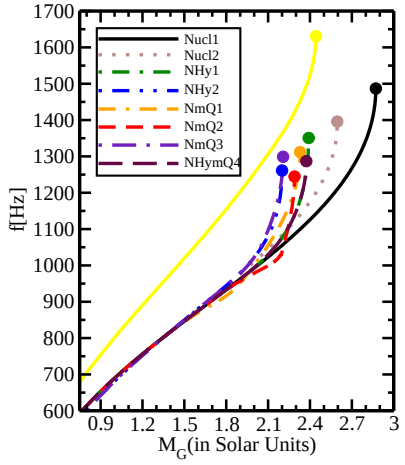

FIG.5

FIG. 5. Keplerian frequency as a function of the gravitational mass.

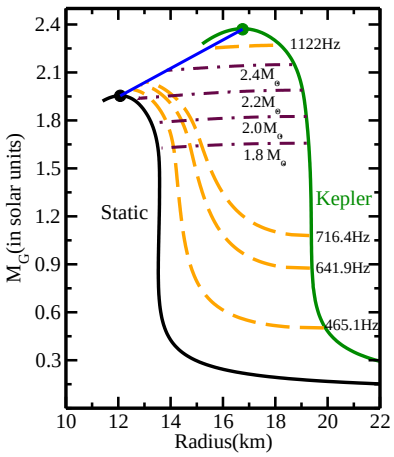

FIG.6

FIG. 6. Gravitational mass (M_G)as a function of the equatorial radius (R_{eq}) for rotating hybrid star. Black solid line in the figure presents static and dark solid green line presents the kepler sequences for NHymQ4 equation of state. The orange dashed lines are at constant frequencies 1122Hz, 716.4Hz, 641.9Hz and 465.1Hz sequences.The horizontal dashed dotted line represents the constant baryon mass sequences at M_B=2.4$M_\odot$, 2.2$M_\odot$, 2.0$M_\odot$, 1.8$M_\odot$.

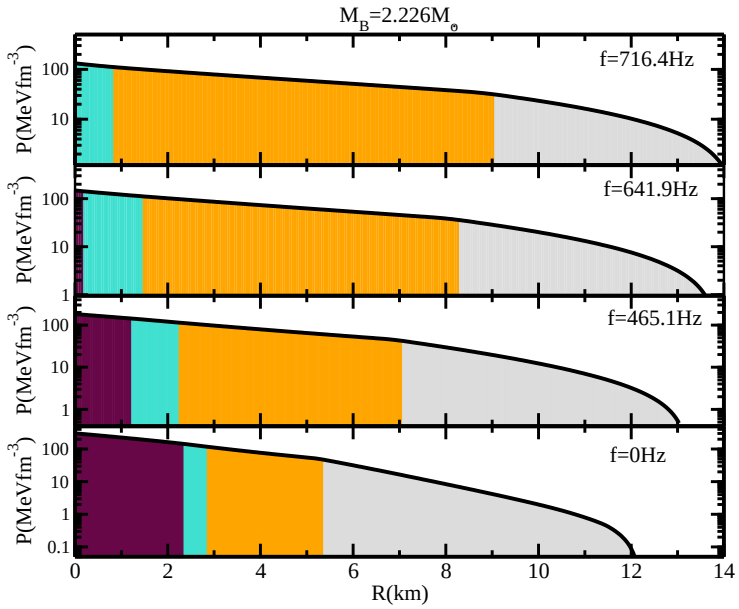

FIG.7

FIG. 7. Equatorial profile of pressure as a function of radial distribution for the non-rotating and spin-down sequences of constant baryonic mass M_B=2.226$M_\odot$ for hybrid star. The chosen spin-down frequencies(f) 716.4Hz, 641.9Hz and 465.1Hz are corresponding to observational limits of the pulsars PSR J1748-2446ad[64], PSR B1937+21[64] and PSR J1903+0327[13, 62] respectively. The grey shaded region represented nucleonic phase only, the orange region represented Hadronic Phase, the turquoise region represented the mixed phase of Hadrons, Hyperons and Quarks. The dark maroon region represented pure quarks in CFL phase.

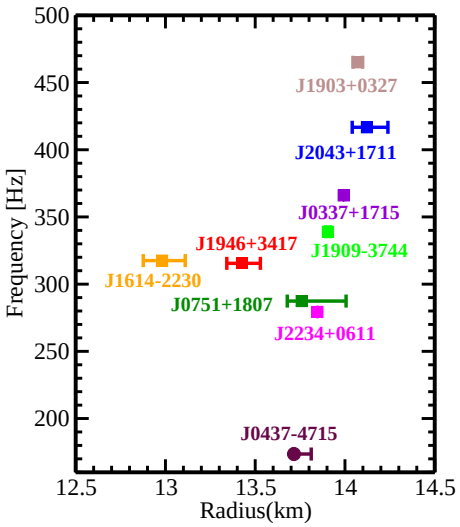

FIG.8

FIG. 8. The theoretical limits of the radii of various well known millisecond pulsars is presented as a function of their rotational frequencies. The theoretical limits of the radii and the gravitational mass of these pulsars have been computed by using NHymQ4 equation of state.

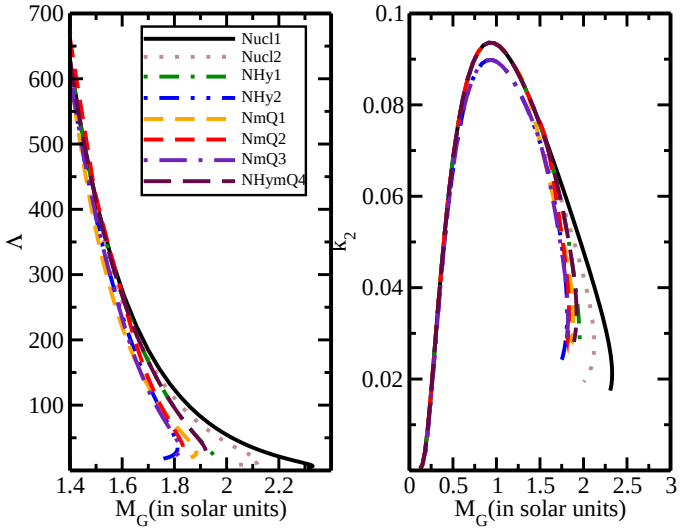

FIG.9

FIG. 9. (Color online) (left panel) The tidal deformability (Λ) and (right panel) the dimensionless Love number (k_2) with respect to gravitational mass for different EOSs.

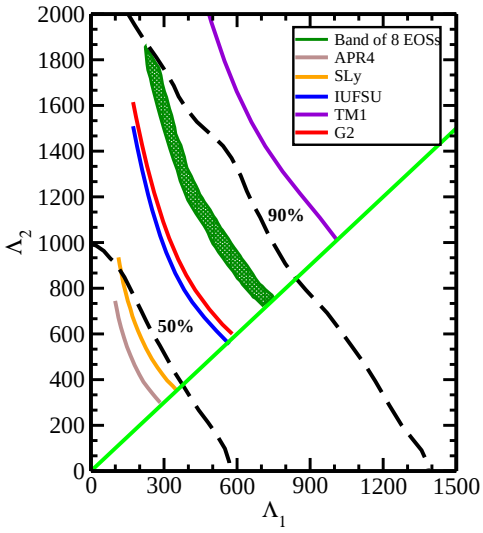

FIG.10

FIG. 10. (Color online) Tidal deformabilities Λ_1 and Λ_2 associated with the high-mass M_1 and low-mass M_2 components of the binary predicted by a set of eight EOSs. The 50% and 90% confidence limits for this event are also indicated.